This is a preprint, the final version is subject to change, of the American Mineralogist (MSA)
Cite as Authors (Year) Title. American Mineralogist, in press.
DOI: https://doi.org/10.2138/am-2018-6282

Pressure, Sulfur and Metal-Silicate Partitioning: The Effect of Sulfur Species on the Parameterization of Experimental Results

*Neil R Bennett & Yingwei Fei

REVISION_1

Geophysical Laboratory, Carnegie Institution of Washington, 5251 Broad Branch Road NW, Washington DC, 20015

*Corresponding Author

Abstract

Performing well-controlled metal-silicate partitioning experiments at conditions directly simulating those of a deep magma ocean is difficult. It is therefore common to perform experiments at lower pressures and temperatures, which are used to determine the effects of salient variables. Often, these effects are determined by multiple linear regression of a dataset covering a large range of *P*-*T*-composition space. In particular, these datasets often contain the results of experiments performed both with and without sulfur in the system. Data are often regressed, however, using a relationship based only upon the formation of oxide species in the silicate melt. Several studies have suggested that, when sulfur is present in the system, siderophile trace metals may also dissolve into silicate melt as S-bearing species. We have derived a relationship for regressing experimental metal-silicate partitioning data that considers the formation of both oxide and sulfide species in the silicate melt. Using model datasets, we have assessed the ability of this relationship, and the more typical single-species relationship, to accurately parameterize data in which the formation of S-bearing species is important. We have also applied this new relationship to experimental results on the metal-silicate partitioning of gold and find

it is able to reconcile the conflicting pressure dependencies of $\ln D_{\mathrm{Au}}^{met/sil}$ found in previous studies.

Keywords: sulfur, core formation, chalcophile, siderophile, speciation, high pressure

1. Introduction

Many studies seek to constrain the conditions of planetary core formation by comparing the composition of primitive mantle (PM) estimated from the rock record with that predicted by forward models based upon experimental results. The experiments used in these forward models equilibrate trace element doped metal and silicate melts at high pressure and temperature, from which metal-silicate partition coefficients $\left(D^{met/sil}\right)$ are determined. Alternatively, for the most siderophile (iron-loving) elements, silicate melts are saturated in the trace element of interest and $D^{met/sil}$ is calculated from the resulting solubility data. Most metal-silicate partitioning data have been produced at pressures below ~27 GPa due to the difficulty of achieving higher pressures using large-volume press techniques. Although these conditions overlap with lower estimates for the maximum depth of core-segregation from a magma ocean (e.g., Li & Agee, 1996; Righter et al., 1997), it is significantly below the maximum pressures invoked in some studies (e.g., 40-80 GPa; Corgne et al., 2009; Rubie et al., 2011; Siebert et al., 2013). Considerable extrapolation of the experimentally determined metal-silicate partition coefficients to relevant conditions is therefore required. This is typically achieved by parameterizing the available data using multiple linear regression, as a function of pressure (P), temperature (T), composition and in some cases oxygen fugacity (fO_2). These parameterizations are based on reactions where the element of interest dissolves in silicate melt as an oxide species. For systems containing sulfur, however, it has been suggested for several elements that the formation of sulfur-bearing complexes is important (e.g. Botcharnikov et al. 2010; Laurenz et al. 2013; Mungall & Brenan, 2014; Bennett et al. 2016). Here, we consider whether these elements require a different

approach to parameterization, to account for the coupled effects of pressure that arise from both the partial molar volume of reaction and changes to the distribution of sulfur between metal and silicate phases. We derive a new form for parameterizing the data from sulfur-bearing experiments and demonstrate the potential for erroneously extrapolating $D^{met/sil}$ with pressure when sulfur-bearing data are parameterized in the traditional manner. We also use existing metal-silicate partitioning data for Au to explore the ability of our new relationship to explain real-world observations. To better test the veracity of this new relationship, however, experiments are needed that target the *P*-*T*-composition conditions and elements for which coupled pressure-sulfur effects are expected to be most apparent.

1.1 Sulfur in Silicate Melts and the Existence of Metal-Sulfur Complexes

Although oxygen is the dominant anion in silicate melts over most terrestrial conditions, sulfur can dissolve in significant quantities as conditions become suitably reducing (≤16 wt % S) (Namur et al., 2016; Wood & Kiseeva, 2016). Below the fayalite-magnetite-quartz buffer (FMQ) sulfur dissolves as S^{2-} and is often considered to replace oxygen bonded to iron (e.g. Mavrogenes & O'Neill, 1999; Métrich et al., 2009). Significant increases in S solubility with more reducing conditions, however, do not manifest until below ~IW -2 and are dependent upon temperature (Namur et al., 2016). As conditions become highly reducing, the sulfur content of silicate melt can exceed the iron content and Namur et al. (2016) suggest in these instances that reaction with Mg and Ca is a significant solution mechanism for S. This assertion is supported by the Raman spectra of silicate melts in equilibrium with sulfide liquid, that display increasingly intense peaks corresponding to MgS and CaS with decreasing fO_2 (IW -3.6 to -8.4) and increasing S content (Namur et al., 2016). Terrestrial core-formation is associated with relatively reducing conditions (fO_2 < IW) and thus metal-silicate partitioning experiments are typically performed at similarly reducing conditions, where sulfur solubility as sulfide species is favored.

The solution of sulfur into silicate melt can potentially affect values of $D^{met/sil}$ for an element, hereafter denoted M, in two ways. The first is via changes to the activity coefficient of oxides species of M in the silicate melt and the second is by bonding with M to form a new, sulfur-bearing, species in the melt. These possibilities are not mutually exclusive, however, and are in fact most likely to operate in tandem. Several authors have presented evidence that the formation of sulfur-bearing species is significant for certain elements. Botcharnikov et al. (2010) investigated the solubility of Au in andesitic and basaltic melts at FMQ -0.4 to +3.3. These authors found an increase in gold solubility in silicate melt with increasing fS_2 for both melt compositions. However, they observed a decrease in sulfide-silicate partition coefficients with ½($\log fO_2$-$\log fS_2$) rather than the expected increase. This effect can be explained by changes to the activity coefficients of Au in sulfide and silicate phases as the fO_2/fS_2 ratio changes, or by challenging the assumption that Au dissolves in the melt strictly as oxide species. Botcharnikov et al. (2010) prefer the latter of these options on the basis of thermodynamic favorability, but are unable to dismiss the former possibility entirely.

The existence of sulfur-bearing Au species was also suggested by Bennett et al. (2016) to explain variations in $D_{Au}^{met/sil}$ with changing S contents in the metal phase. These authors observed a decrease in $D_{Au}^{met/sil}$ with increasing sulfur content of the metal. This behavior is expected on the basis of previous work in solid metal-liquid metal systems that shows the affinity of gold for metal decreases as the non-metal content of the metal increases (Jones & Malvin, 1990; Chabot & Jones, 2003). The magnitude of this decrease, however, was greater than expected on the basis of known activity-composition relationships in the metal phase. This result can be explained either by changes to activity-composition relations in the silicate melt as S is added, and/or by the formation of sulfur-bearing Au species. The dependence of $D^{met/sil}$ on $\log fS_2$ found by Bennett et al. (2016) does not support the

formation of a simple Au_2S species, consistent with the findings of Botcharnikov et al. (2010). Bennett et al. (2016) thus similarly conclude that either more complex Au species in the silicate melt are required, or the activity coefficients of Au species in the silicate melt depend strongly on composition.

Laurenz et al. (2013) investigated the solubility of Pd and Ru in both sulfur-bearing and sulfur-free picritic melts over a range of fO_2. They found that Ru and Pd dissolve as 4+ and 1+ species respectively, at oxygen fugacities within several log units of the FMQ buffer. The solubility of Ru was found to be higher in the sulfur-bearing system (log fS_2 = -2.3) by approximately one order of magnitude at similar fO_2, which the authors attribute to the formation of RuS_2 species in the silicate melt. Pd solubility was seen to decrease with the addition of sulfur to the system, however, due to a reduction in Pd activity as Pd metal reacted with S to form a Pd-Fe-S melt (Laurenz et al., 2013). Mungall & Brenan (2014) used the results of Laurenz et al. (2013) for Ru, alongside their own experimental data for Pt and Ir, to estimate ΔG_r^o for the formation of metal-sulfur complexes in the silicate melt *via* reactions of the form: $MO_{n/2}\ (sil) + \frac{n}{4}S_2\ (g) = MS_{n/2}\ (sil) + \frac{n}{4}O_2\ (g)$. Their analysis permits the alloy solubility to be estimated as a function of fO_2 and fS_2, and reveals that sulfur enhances solubility for all three metals.

Wood & Kiseeva (2016) determined sulfide-silicate partition coefficients for a range of lithophile elements and copper, across a very broad range of fO_2. In their most reducing experiments the authors observed a dramatic increase in the sulfur solubility of the silicate melt and concomitant decrease in $D^{sulf/sil}$ for copper by approximately an order of magnitude. As with Au and Ru discussed above, Cu is a strongly chalcophile element, and thus may also be susceptible to the formation of sulfur-bearing complexes in silicate melt. However, it is also possible that this change in the partitioning behavior is bought about by changes to the activity-composition relations resulting from the increased sulfur

121 contents of the silicate melt.

122

123 From the brief summary above, it is clear that sulfur dissolved into silicate melts affects the solubility
124 and partitioning of certain, typically chalcophile, trace elements. Despite this, it is hard to claim the
125 existence of metal-sulfide species in silicate melts from only solubility and partitioning measurements.
126 Spectroscopy, however, can provide direct evidence for the formation of these species in silicate melt.
127 Evans et al., (2009) performed X-ray absorption near edge structure (XANES) analysis of quenched
128 silicate glasses synthesized at 1673 K, and controlled fO_2, fS_2 conditions (predominantly FMQ -3.2 and
129 $\log fS_2$ = -1.91). Starting materials were powdered mixtures with compositions in the CMAS system
130 (CaO-MgO-Al_2O_3-SiO_2), to which variable amounts of Mn, Ni and W were added. On the basis of
131 changes to the composite peak observed in sulfur K-edge XANES spectra, Evans et al., (2009)
132 recognized the formation of Mn-S species in their silicate melts and found that the formation of W-S
133 species was also consistent with their spectroscopic results. The low S contents of Ni-bearing melts,
134 due to saturation in an immiscible NiS phase, results in a low signal to noise ratio of the spectra and
135 prevents the possible identification of Ni-S species. The authors calculate that no more than ~20% of
136 Mn and ~2% of W are dissolved as sulfide species at the conditions of their experiments, which contain
137 ~0.2 wt% sulfur. It is noteworthy that the platinum group metals, Cu, and Au, as discussed earlier, are
138 all more chalcophile than Mn or W and thus may be expected to more readily form sulfide species in
139 the silicate melt. Furthermore, conditions in the Evans et al., (2009) experiments are more oxidizing
140 than those employed in metal-silicate partitioning experiments designed to study core formation (i.e.,
141 they are above the iron-wüstite buffer). At more reducing conditions, where S concentrations in the
142 silicate melt may be higher, it is reasonable to expect that metal-sulfur species will compose an even
143 greater proportion of the dissolved metal content.

144

145 Finally, we emphasize that the formation of metal-sulfur species does not diminish the importance of

activity-composition relations in both the metal and silicate phases with respect to element partitioning. The complexity that can arise due to some of these effects is discussed in detail by Jana & Walker (1997) in their study of trace element partitioning behavior as a function of sulfur content. In particular, these authors note that strong non-ideality in the Fe-S system permits a situation where increasing X_{S}^{bulk} leads to a decrease in X_{S}^{sil} when $X_{\mathrm{S}}^{met} > X_{\mathrm{Fe}}^{met}$. Addition of sulfur to the system beyond the amount required to form stochiometric FeS will, by necessity, consume Fe from the silicate melt to form additional FeS and thus increase the mass fraction of sulfide. This decrease in X_{Fe}^{sil} leads to a concomitant decrease in X_{S}^{sil} as Fe is the dominant complexing agent for S in the silicate melt. Maintaining the requirement $a_{\mathrm{S}}^{met} = a_{\mathrm{S}}^{sil}$ as X_{S}^{bulk} increases and X_{S}^{sil} decreases therefore necessitates significant changes to $\gamma_{\mathrm{S}}^{sil}$. The authors also note that an analogous situation will arise for metals other than Fe in the silicate melt, explaining their observation that partition coefficients for elements such as Au and Ni increase sharply in their highest S experiments. To avoid some of these complexities in the present study, our discussion will only consider metallic melts that are more Fe-rich than the Fe-FeS eutectic.

2. Theoretical Considerations

2.1 A Typical Relationship for Parameterizing $D^{Met/Sil}$

The dissolution of a trace metal (M) into silicate melt is typically considered in terms of the following heterogeneous reaction:

$$\mathrm{M}\ (met) + \tfrac{n}{4}\mathrm{O}_2\ (g) = \mathrm{MO}_{n/2}\ (sil) \qquad (1)$$

where *n* is the oxidation state of the metal when dissolved in the melt. The equilibrium constant for this reaction (K_1) is as follows:

$$K_1 = \frac{a_{MO_{n/2}}^{sil}}{a_M^{met} f\mathrm{O}_2^{n/4}} \qquad (2)$$

where a_i^{α} is the activity of species i in phase α and fO_2 is the oxygen fugacity. Expanding the activity terms (given: $a_i^{\varepsilon} = \gamma_i^{\varepsilon} X_i^{\varepsilon}$) and taking the natural log, equation 2 becomes:

$$\ln K_1 = -\frac{n}{4}\ln fO_2 + \ln\left(\frac{X^{sil}_{\mathrm{MO}_{n/2}}}{X^{met}_{\mathrm{M}}}\right) + \ln\left(\frac{\gamma^{sil}_{\mathrm{MO}_{n/2}}}{\gamma^{met}_{\mathrm{M}}}\right) \qquad (3)$$

where X_i^{ε} and γ_i^{ε} are the mole fraction and activity coefficient of i in phase ε respectively. The Gibbs free energy of reaction (ΔG_r^o) is related to the equilibrium constant through the following relationship:

$$\Delta G^o_{r1} = -RT\ln K_1 \qquad (4)$$

Substituting (3) into (4) and rearranging yields:

$$\frac{\Delta G^o_{r1}}{-RT} = -\frac{n}{4}\ln fO_2 + \ln\left(\frac{X^{sil}_{\mathrm{MO}_{n/2}}}{X^{met}_{\mathrm{M}}}\right) + \ln\left(\frac{\gamma^{sil}_{\mathrm{MO}_{n/2}}}{\gamma^{met}_{\mathrm{M}}}\right) \qquad (5)$$

The molar metal-silicate partition coefficient of metal M ($D_{M1}^{met/sil}$) is defined by the following ratio:

$$D^{met/sil}_{\mathrm{M1}} = \frac{X^{met}_{\mathrm{M}}}{X^{sil}_{\mathrm{MO}_{n/2}}} \qquad (6)$$

Rearranging (5) in terms of $\ln D^{met/sil}_{\mathrm{M1}}$ and remembering that $\Delta G_r^o = \Delta H_r^o - T\Delta S_r^o + P\Delta V_r^o$ yields:

$$\ln D^{met/sil}_{\mathrm{M1}} = \frac{\Delta H_r^o}{RT} - \frac{\Delta S_r^o}{R} + \frac{P\Delta V_r^o}{RT} - \frac{n}{4}\ln fO_2 + \ln\left(\frac{\gamma^{sil}_{\mathrm{MO}_{n/2}}}{\gamma^{met}_{\mathrm{M}}}\right) \qquad (7)$$

Equation 7 provides the thermodynamic basis of equations used to parameterize experimental metal-silicate partitioning data. The entropy, enthalpy, and molar volume terms are typically replaced with fitting parameters (denoted here as a, b and c, respectively), that allow the pressure and temperature dependence of partitioning to be described. The oxidation state (n) of M when dissolved in silicate melt can be determined either from the dependence of $\ln D_M^{met/sil}$ on $\ln fO_2$ in experiments at constant P and T, from spectroscopic measurements of quenched glasses (e.g. XANES), or inferred from the stability of end-member oxides. The treatment of metal and silicate activity terms varies between studies. For the present study, we will use the simple implementation of Jones & Malvin (1990) to describe interactions with S in the metal phase (i.e. to describe changes in $\gamma^{met}_{\mathrm{M}}$). We note, however, that this

183 approach may not be adequate for complex alloy compositions and an implementation such as that
184 described by Ma (2001) may provide greater accuracy. For simplicity, ideality will be assumed for the
185 silicate melt $\left(\gamma^{Sil}_{\mathrm{MO}_{n/2}} = 1\right)$, however, it is likely that non-ideal interactions in the silicate melt will be
186 important in some cases. Implementing these amendments to (7) results in the following relationship:

$$\ln D^{met/sil}_{\mathrm{M1}} = a_1 + \frac{b_1}{T} + \frac{c_1 P}{T} - \frac{n}{4}\ln fO_2 + \beta\ln(1 - 2\alpha X^{met}_{\mathrm{S}}) \qquad (8)$$

187 where β is the M-S interaction parameter and α is a constant specific to the compositional system being
188 studied. Strictly, (8) only describes the equilibrium shown in (1) and is therefore only a complete
189 description of the metal-silicate partitioning if M forms a single oxide species in the silicate melt across
190 the range of conditions being studied. The formation of multiple oxide species (i.e., *n* does not have a
191 single value), or sulfur-bearing species is thus not rigorously accounted for by a relationship such as
192 (8). Relationships such as this have often been applied to parameterize datasets containing both sulfur-
193 bearing and sulfur-free experiments (e.g. Righter et al., 1997; Righter & Drake, 1997; Li & Agee, 2001;
194 Chabot & Agee, 2003; Mann et al., 2009; Righter et al., 2015). However, evidence for the formation of
195 metal-sulfur complexes in silicate melts suggests that, for certain elements, this may not be an entirely
196 valid approach. To help assess the veracity of parameterizing data in this manner, a modified
197 relationship is derived in the following section that accounts for the formation of multiple species.
198
199 **2.2 Developing a Relationship that Considers Sulfide Species**
200 The solution of M into silicate melt to form sulfide species can be described using a heterogeneous
201 reaction analogous to (1) for the formation of oxide species:

$$\mathrm{M}\,(met) + \frac{n}{4}\mathrm{S}_2\,(g) = \mathrm{MS}_{n/2}\,(sil) \qquad (9)$$

202 Taking the equilibrium constant of (9) and following the same procedure as outlined in equations 2-8,
203 we arrive at the following expression for the molar partition coefficient concerned with sulfide species
204 in the silicate melt:

$$\ln D_{\mathrm{M9}}^{met/sil} = a_9 + \frac{b_9}{T} + \frac{c_9\ P}{T} - \frac{n}{4}\ln f\mathrm{S}_2 + \beta\ln(1 - 2\alpha X_{\mathrm{S}}^{met}) \qquad (10)$$

Note that in (10), the activity coefficient of the sulfide species in silicate melt is again assumed to be equal to 1. Equation 6 and the analogous relationship for reaction 9 describe the species-specific partitioning of M, which can be combined to yield a bulk partition coefficient $\left(D_{\mathrm{M}bulk}^{Met/Sil}\right)$:

$$\frac{1}{D_{\mathrm{M}bulk}^{met/sil}} = \frac{X_{\mathrm{MO}_{n/2}}^{sil} + X_{\mathrm{MS}_{n/2}}^{sil}}{X_{\mathrm{M}}^{met}} = \frac{1}{D_{\mathrm{M1}}^{met/sil}} + \frac{1}{D_{\mathrm{M9}}^{met/sil}} \qquad (11)$$

Substituting the exponents of (8) and (10) into (11), taking the logarithm and simplifying using the identity $\ln(x + y) = \ln x + \ln\left(1 + \frac{y}{x}\right)$, yields:

$$\ln D_{\mathrm{M}bulk}^{met/sil} = a_1 + \frac{b_1}{T} + \frac{c_1\ P}{T} - \frac{n}{4}\ln f\mathrm{O}_2 + \beta\ln(1 - 2\alpha X_{\mathrm{S}}^{met}) - \ln\left(1 + \frac{e^{a_1 + \frac{b_1}{T} + \frac{c_1 P}{T}}}{e^{a_9 + \frac{b_9}{T} + \frac{c_9 P}{T}}} \cdot \frac{\left(f\mathrm{S}_2\right)^{\frac{n}{4}}}{\left(f\mathrm{O}_2\right)^{\frac{n}{4}}}\right) \qquad (12)$$

Equation (12) can be used to describe the bulk partitioning of M, assuming ideal behavior for the dissolved oxide and sulfide components of M in the silicate melt. Similar to the case for sulfide-silicate partitioning, (12) includes an $f\mathrm{S}_2/f\mathrm{O}_2$ term that can be difficult to evaluate in high pressure experiments. To include the effects of this term in a more tractable manner, we make several alterations to (12) in order to derive an expression that is useful for the regression of high *P*-*T* experimental data.

The dissolution of sulfur (as S^{2-}) into silicate melt by replacement of oxygen is represented by the following reaction:

$$\mathrm{O}^{2-}(sil) + \frac{1}{2}\mathrm{S}_2\ (g) = \mathrm{S}^{2-}(sil) + \frac{1}{2}\mathrm{O}_2\ (g) \qquad (13)$$

Because the concentration of O^{2-} in silicate melt far outweighs that of any other anion, it can be considered constant. With this approximation, a modified equilibrium constant can be written for (13) termed the sulfide capacity (C_{S}) of the melt (Mavrogenes & O'Neill, 1999):

$$C_{\mathrm{S}} = X_{\mathrm{S}}^{sil}\left(\frac{f\mathrm{O}_2}{f\mathrm{S}_2}\right)^{\frac{1}{2}} \qquad (14)$$

221 Remembering that the molar metal-silicate partition coefficient for sulfur is:

$$D_{\mathrm{S}}^{met/sil} = \frac{X_{\mathrm{S}}^{met}}{X_{\mathrm{S}}^{sil}} \qquad (15)$$

222 Casting (15) in terms of X_{S}^{Sil}, substituting into (14), then rearranging:

$$\left(\frac{X_{\mathrm{S}}^{met}}{C_{\mathrm{S}}D_{\mathrm{S}}^{met/sil}}\right)^2 = \frac{f\mathrm{S}_2}{f\mathrm{O}_2} \qquad (16)$$

223 The left hand side of (16) can be used to replace the $f\mathrm{S}_2/f\mathrm{O}_2$ term in (12), to yield the following
224 relationship:

$$\ln D_{\mathrm{M}bulk}^{met/sil} = a_1 + \frac{b_1}{T} + \frac{c_1 P}{T} - \frac{n}{4}\ln f\mathrm{O}_2 + \beta\ln(1 - 2\alpha X_{\mathrm{S}}^{met}) - \ln\left(1 + \frac{e^{a_1+\frac{b_1}{T}+\frac{c_1 P}{T}}}{e^{a_9+\frac{b_9}{T}+\frac{c_9 P}{T}}}\cdot\left(\frac{1}{C_{\mathrm{S}}}\right)^{\frac{n}{2}}\cdot\left(\frac{X_{\mathrm{S}}^{met}}{D_{\mathrm{S}}^{met/sil}}\right)^{\frac{n}{2}}\right) \qquad (17)$$

225 We consider it useful to replace X_{S}^{sil} with $X_{\mathrm{S}}^{met}/D_{\mathrm{S}}^{met/sil}$ as this form is most useful for employing the
226 relationship in forward models of core formation, in which values for X_{S}^{sil} and X_{S}^{met} should be related
227 by $D_{\mathrm{S}}^{met/sil}$ and it is the light element content of the metal that is often defined. For typical values of
228 the coefficients *a*-*c*, and the *P*-*T* range salient to metal-silicate partitioning experiments, changes to
229 $\frac{e^{a_1+\frac{b_1}{T}+\frac{c_1 P}{T}}}{e^{a_9+\frac{b_9}{T}+\frac{c_9 P}{T}}}\cdot\left(\frac{1}{C_{\mathrm{S}}}\right)^{\frac{n}{2}}$ with *P* and *T* remain relatively small, and thus we are able to replace this term with
230 $\left(d/X_{\mathrm{FeO}}^{sil}\right)^{n/2}$, where *d* is a fitting parameter, without incurring significant inaccuracies in the fitted
231 values of b_1 and c_1; the temperature and pressure dependence of partitioning respectively. The sulfide
232 capacity (C_{S}) depends upon melt composition and $f\mathrm{O}_2$ (e.g., Namur et al., 2016) and hence we include
233 X_{FeO}^{sil} in our new fitting term, which is a proxy for $f\mathrm{O}_2$ in metal-silicate partitioning experiments and the
234 only silicate melt component that varies in the synthetic data. Further discussion of the simplifications

made in this section, and their efficacy, is provided in section 3. Following this replacement, we arrive at:

$$\ln D_{\mathrm{M}bulk}^{met/sil} = a_1 + \frac{b_1}{T} + \frac{c_1 P}{T} - \frac{n}{4}\ln fO_2 + \beta\ln(1 - 2\alpha X_{\mathrm{S}}^{met}) - \ln\left(1 + \left(\frac{d}{X_{\mathrm{FeO}}^{sil}}\right)^{\frac{n}{2}}\left(\frac{X_{\mathrm{S}}^{met}}{D_{\mathrm{S}}^{met/sil}}\right)^{\frac{n}{2}}\right) \quad (18)$$

Equation 18 thus provides a form for parameterizing experimental data for elements that dissolve as both oxide and sulfide species in silicate melt. Note that in fits to real experimental data, values of *d* may contain a contribution from activity-composition effects that are not otherwise explicitly accounted for. Because the metal-silicate partitioning of sulfur $\left(D_{\mathrm{S}}^{met/sil}\right)$ and metal activity terms are constrained independently, rather than fit to the experimental data, the number of fitting parameters remains relatively small. Where possible, *b* can also be independently constrained from end-member thermodynamic data, further reducing the number of fit parameters (e.g. Wade & Wood 2005).

2.3 Physical Interpretation of the Functional Form

Figure 1 displays $\ln D_{\mathrm{M}}^{met/sil}$ as a function of pressure for a hypothetical 2+ cation (n = 2) that forms both sulfide and oxide species in the silicate melt. Temperature is fixed at 2500 K and the metal is assumed to contain 20 mol% sulfur. Values for the parameters *a*, *b*, and *c*, are fixed at 1, 10,000, -50 respectively. The value of *d* is varied between 0 and 20, as indicated for each curve. For the present study, we have parameterized the value of $\ln D_{\mathrm{S}}^{met/sil}$ as a function of P, X_{FeO}^{sil}, X_{S}^{met} and $\sum X_i^{met}$ where *i* = Si, O, C, P. The inclusion of a $1/T$ term for parameterizing $\ln D_{\mathrm{S}}^{met/sil}$ was found to be insignificant at the 95% confidence level. Our regression yields a pressure effect which is similar in magnitude to the studies of Rose-Weston et al. (2009) and Boujibar et al. (2014), but significantly larger than the study of Sauer et al. (2017), which includes the results of diamond anvil cell experiments. Details of this

parameterization are provided in the supplement to this manuscript.

Clear from Fig. 1 is that when $d \neq 0$ (i.e., when M-S species are formed in the silicate) the metal-silicate partition coefficient first increases then decreases with increasing pressure. This behavior results from the competing effects of the partial molar volume of reaction and changes to the mole fraction of sulfur in silicate melt arising from sulfur's more siderophile behavior with increasing pressure. For transition metal cations (e.g. Ni, Co, Mn, W, Zn, Mo), the c term, related to ΔV_r^o, is often found to be negative (Wade & Wood, 2005; Siebert et al., 2011). This suggests that higher pressures favor more lithophile behavior for these elements. Higher pressures, however, result in more siderophile behavior for sulfur; lowering the concentration of S^{2-} in the silicate melt and reducing the propensity to form dissolved $MS_{n/2}$ species. By removing this solution mechanism, M behaves in a relatively more siderophile fashion as pressure is increased. It is the competition between these effects that results in the curvilinear pressure dependence of $\ln D_{\mathrm{M}}^{met/sil}$ predicted by equation 18. The inflection point in the curve thus indicates the pressure at which partial molar volume effects become dominant over the changing S concentration in silicate melt. At pressures above this inflection point M will be dissolved in silicate melt primarily as the oxide species, due to the low S concentrations in the melt at high pressure. At these conditions, it is therefore the dependence of the oxide-forming reaction on pressure that controls the partitioning behavior of M. The location of the inflection point will depend upon the partitioning behavior of sulfur, in concert with the *P-T-X* dependencies of the individual metal-oxide and metal-sulfide species. It is worth noting that at extremely reducing conditions, the dominant complexing agent for S in the silicate melt may be Ca or Mg, rather than Fe (Namur et al., 2016). The pressure dependence for the metal-silicate partitioning of sulfur determined at more oxidizing conditions may therefore not apply in these instances. If sulfur concentrations in the silicate are not dramatically reduced with pressure, due to changes in S speciation at very low fO_2, the

situation described above for trace element M might look quite different.

3. Assessment of Parameterization Forms

The observation that (18) predicts a non-linear change in $\ln D_{\mathrm{M}}^{met/sil}$ with pressure suggests that fitting data with a relationship such as (8) may yield inaccurate extrapolation of experimental data to higher pressures, especially when the experimental data do not cover a sufficiently large range. This may occur despite an apparently good fit to the experimental data on plots of the measured *versus* predicted partition coefficients (i.e., close to a 1:1 correlation is observed). This may be particularly problematic when experiments contain complex metal alloy compositions and activity-composition effects are included as parameters in the regression. In these instances, the large number of fitting parameters, coupled with the covariance between intensive variables common to high pressure experiments, can make it difficult to assign unique values to fitting parameters. If the relationship used to parameterize the data does not have the appropriate functional form, it is foreseeable that parameters will be skewed from their true values.

3.1 Application to Model Data

3.1.1 Model Inputs. To assess the differences that arise from using different parameterizations for data concerning elements that may form M-S and M-O species, we generated model datasets using (8), (10) and (11), that were then regressed using (8) and (18). Note that although (8) is used for both the creation and regression of the model data, circularity is avoided as each model datapoint also depends upon the evaluation of (10). For each model dataset, values for the coefficients (*a, b* and *c*) were selected from the ranges shown in Table 1, which reflect typical values from the literature for the metal-silicate partitioning of transition metal cations. Further details regarding the exact coefficients used are provided in subsequent sections. To simulate a realistic degree of scatter within each dataset *a*,

303 *b* and *c* are assigned errors of ±0.1, ±500 and ±20 respectively. Values of $\ln D_{\mathrm{M}}^{met/sil}$ for each model
304 datum are then calculated by selecting values for *a*-*c* at random from the defined ranges; i.e., within
305 error of the nominal value. Pressures and temperatures are selected for each datum from ranges of 0.1
306 MPa – 27 GPa and 1473 – 2673 K, to encompass the range of conditions accessible by one atmosphere
307 furnace, piston-cylinder and multi-anvil experimental equipment. Because pressure and temperature are
308 typically coupled to some degree in petrological experiments, the following relationships are used to
309 capture the spread of conditions observed in the literature:

$$T(\mathrm{K}) = 1800 \pm 50 \quad 0.1\ \mathrm{MPa} < P < 0.5\ \mathrm{GPa} \qquad (19)$$

$$T(\mathrm{K}) = 2150 \pm 300 + 2P(\mathrm{GPa}) \quad 0.5\ \mathrm{GPa} < P < 10\ \mathrm{GPa} \qquad (20)$$

$$T(\mathrm{K}) = 2373 \pm 300 + 2P(\mathrm{GPa}) \quad 10\ \mathrm{GPa} < P < 27\ \mathrm{GPa} \qquad (21)$$

310 It is also common for experimental datasets to contain a larger proportion of results at low *P* relative to
311 high *P*, due to the greater ease of performing experiments at lower *P*. To incorporate the effect of this
312 bias, randomized selection of pressures for the model data is weighted towards low *P* using the positive
313 region of a Gaussian distribution with values of 0 and 8 chosen for the mean and standard deviation
314 respectively. Oxygen and sulfur fugacity are linked by the following equilibrium:

$$\mathrm{FeO}\ (sil) + \tfrac{1}{2}\mathrm{S}_2\ (g) = \mathrm{FeS}\ (sil) + \tfrac{1}{2}\mathrm{O}_2\ (g) \qquad (22)$$

315 and thus are expected to show a sympathetic variation. In the model, X_{S}^{met} is chosen at random from a
316 value between 0 and the Fe-FeS eutectic composition at *P*. Using this value and the independently
317 known metal-silicate partition coefficient of sulfur X_{S}^{sil} can be defined, from which X_{FeS}^{sil} is calculated
318 using the conversion factor listed in Table 1 for a basaltic melt composition. X_{FeO}^{sil} is either fixed for all
319 datapoints (initial models) or given a randomly selected value of 0.02 – 0.15, to ensure several log units
320 variation in fO_2 within each dataset (later models). The reaction Fe (met) + ½S_2 (*g*) = FeS (*sil*) is then
321 used to define the fS_2, with ΔG_r^o taken from the NIST-JANAF thermochemical tables (Chase et al.
322 1985). Activity coefficients for iron in Fe-S alloys are calculated as a function of *P*, *T* and composition

using the model of Buono & Walker (2011). This approach ensures that each model datum is self-consistent in the definition of alloy composition, silicate liquid composition and the fO_2, fS_2 terms. Oxygen fugacity for each model datum is calculated relative to the iron-wüstite buffer (ΔIW) using the following relationship:

$$\Delta\mathrm{IW} = 2\log\left(\frac{a_{\mathrm{FeO}}^{sil}}{a_{\mathrm{Fe}}^{met}}\right) \qquad (23)$$

Ideality is assumed for FeO in the silicate melt and non-ideal behaviour in the Fe-S alloy is accounted for using the model of Buono & Walker (2011). This calculation suggests oxygen fugacity ranges between ~IW -4 to -1.2 for the model data.

3.1.2 Results of Fitting Synthetic Data: Fixed *P-T* Dependency. The primary focus of this study is to assess inaccuracies that might result when metal-silicate partitioning data are parameterized using a relationship that only considers oxide species, when there is the potential for both oxide and sulfur-bearing species to be dissolved in silicate melt. To this end, 100 model datasets were generated with values of *a, b, c* and *n* that yield a large value for $\frac{d^2 D_M^{met/sil}}{dP^2}$ (i.e., a strong curvature in the trend when $\ln D_{\mathrm{M}}^{met/sil}$ is plotted against pressure). Initially, the values chosen were; a_1 = 1, a_2 = -2.5, b_1 = 8000, b_2 = 3000, c_1 = -70, c_2 = -50. The effect of different choices will be explored below. Each dataset comprises 50 datapoints. Figs 2a and 2b show the distribution of model data with respect to *P*, *T*, and X_S (*met*). Fig 2c displays the distribution of values for a_1-c_1 found by regression of the data using (8) (blue points) and (18) (red points). Fig 2d displays the nominal values of $\ln D_{\mathrm{M}}^{met/sil}$ *versus* those predicted by the model fits, color-coded in the same manner as for Fig 2c.

From Fig 2d, it is apparent that (18) better reproduces the model data, which is to be expected given the extra fitting parameter. Comparison of the adjusted R^2, however, confirms that (18) yields an improved

345 fit to the model data even after accounting for the number of fitting parameters (average adjusted R^2 =
346 0.999 *vs* 0.995). Inspection of only the blue points in Fig 2d reveals that, despite yielding a worse fit to
347 the data than (18), the relationship considering only oxide species (8) still generates fits that place data
348 close to the one-to-one line and have high R^2 values. Often, these metrics are used to demonstrate that
349 model parameterizations are able to adequately recreate the experimental data (e.g. Righter et al., 2011;
350 Righter et al., 2015). Fig 2c, however, reveals that the parameters a_1-c_1 are in many cases not
351 representative of those used to generate the model data. The accuracy of extrapolations made outside
352 the *P*-*T* range of the data is therefore called into question. Figure 3 shows *P* versus $\ln D_M^{met/sil}$ as
353 predicted by (8) and (18), blue and red curves respectively, at 2500 K and X_S = 0.2. Predictions made
354 on the basis of Equation (18) generally come close to reproducing the model data (thick black curve),
355 whereas predictions made on the basis of (8) typically overestimate $\ln D_M^{met/sil}$ at pressures above and
356 below the apex of the actual pressure dependence. In many cases, the c_1 term found by regression of the
357 data using (8) is opposite in sign to the nominal value used to generate the data. This leads to
358 significant overestimation of $\ln D_M^{met/sil}$ in extrapolations to the highest pressures associated with core
359 formation (i.e. 40-80 GPa). Despite the improvement found by using (18), Fig 3 reveals that at low *P*
360 (<10 GPa) values of $\ln D_M^{met/sil}$ are slightly overpredicted. This mismatch arises from differences
361 regarding how activity-composition relationships are accounted for in the relationship for metal-silicate
362 partitioning of sulfur, as used to regress the data, versus how they are incorporated into the calculation
363 of fO_2 and fS_2, as used to generate the model datapoints. It is therefore worth noting that the
364 relationship employed for $\log D_S^{met/sil}$ bears strongly on the accuracy of the parameterization made
365 using (18). As controls over the value of $\log D_S^{met/sil}$ become increasingly better constrained, it is
366 reasonable to expect the range of conditions over which (18) can be reliably employed will grow
367 accordingly.
368

Although the above procedure demonstrates that not accounting for sulfur-bearing species has the potential to affect the accuracy of extrapolations made on the basis of parameterized data, not all situations will give rise to such a dramatic effect. It is expected that the degree of curvature observed in the pressure dependence of $\ln D_{\mathrm{M}}^{met/sil}$ will depend upon the enthalpy, entropy and molar volume contributions to each species-specific partition coefficient. In particular, as the contribution of sulfur-bearing species to the total dissolved load of M in the silicate melt decreases, the partitioning behavior should more closely approach that expected for reaction (1). Generating trends with (11) for which a_1 = 4, $b_1 = b_9$ = 5000, $c_1 = c_9$ = -100, and a_9 is varied from -4 to +4 (where the contribution from sulfur-bearing species increases as a_9 increases), then plotting P versus $\ln D_{\mathrm{M}}^{met/sil}$ for a 2+ cation at conditions of 2500 K and X_{S} = 0.2, shows that this expectation is borne out (Fig 4). Therefore, in instances where $X_{\mathrm{MSn/2}} << X_{\mathrm{MO}n/2}$, using relationship (8) to parameterize the data is unlikely to result in problems during extrapolation. It is noteworthy that situations have already been described in the literature where $X_{\mathrm{MSn/2}} >> X_{\mathrm{MO}n/2}$, and thus non-linear changes in $\ln D_{\mathrm{M}}^{met/sil}$ with P might be expected. For example, on the basis of Ru solubility experiments, Laurenz et al., (2013) estimate that Ru is nearly 1000 times more likely to associate with S^{2-} than O^{2-} at an fO_2 close to the fayalite-magnetite-quartz buffer.

3.1.3 Results of Fitting Synthetic Data: Variable *P-T* Dependency. To assess the efficacy of (8) and (18) in accurately parameterizing data across a broad spectrum of *P-T-X* dependencies, element oxidation state, and number of datapoints, 2000 model datasets were generated using randomly selected values of a, b, c, n and β from the ranges in Table 1. The number of datapoints per dataset was varied between 15 and 150. Unlike the initial fitting test described at the start of the section, this set of models is designed to probe which regions of parameter space are likely to result in inaccurate fits, and also to test the validity of including the d parameter in place of a more complex (but potentially more accurate)

term that includes a *P*-*T* dependence. A further difference with these models is the inclusion of an uncertainty on the metal activity term, β, of ±0.1.

Fig 5a displays a comparison between the actual values of a_1-c_1 and those generated by fits with (8) and (18), as a function of the number of datapoints in each dataset. Surprisingly, datasets with more individual datapoints do not display a significant improvement in the accuracy of fit. It is clearly apparent, however, that fits made using (8) systematically over-estimate the value of the pressure dependence for $\ln D_{\mathrm{M}}^{met/sil}$. Plotted in Fig 5b is comparison between the fit accuracy and the absolute values of a_1-c_1. As might be expected, weak nominal pressure and temperature dependencies (i.e., small values of b_1 and c_1) leads to greater inaccuracy in the fitted parameters for these variables, regardless of whether (8) or (18) is used. Also noteworthy is that fitted values of a_1 tend to be underpredicted, particularly when nominal values of a_1 are > 0. Fitted values of a_1 have little effect on extrapolations made to different *P*-*T* conditions, however, and are thus less important to the present discussion.

In §2.2, we noted that the fitting parameter *d* includes a contribution from the ratio $\frac{e^{a_1+\frac{b_1}{T}+\frac{c_1 P}{T}}}{e^{a_9+\frac{b_9}{T}+\frac{c_9 P}{T}}}$ (hereafter denoted R_{G}), and thus fits to datasets where this ratio varies significantly might suffer inaccuracies. Fig 5c displays values of a_1-c_1 found using (18) compared to the input values, as a function of the range in R_{G} displayed by a given dataset. Values of R_{G} are small for most of our model datasets, due to the protocol used to generate the data. To help 'see-through' this sampling bias, results were binned by intervals of 2 in R_{G}, then 15 datasets were selected at random from each bin for display in Fig 5c. Data are only shown up to values of R_{G} = 15, as for higher values, less than 15 datasets are present in each bin. It is clear from Fig 5 that, for most datasets, values of a_1-c_1 found by (18) agree well with the nominal values (i.e., lie close to 0 on the ordinate axis) and no systematic changes in the quality of fit are observed as a function of R_{G}. This result suggests that the simplification made by introducing *d* in

417 place of a *P-T* dependent term is permissible, at least for the range of *a-c* coefficients and *P-T* space
418 considered here. Fig 5d displays the accuracy of a_1-c_1 determined from (8) and (18) as a function of the
419 range in sulfur content exhibited by the dataset. As the range in sulfur content between experiments
420 increases, there is a general worsening in the accuracy of a_1-c_1 found using both parameterizations. In
421 particular, determination of the c_1 parameter suffers significantly when the range of S contents is
422 largest, being generally higher or lower than the nominal value when using (8) and (18) respectively.
423
424 Following the discussion in the previous sections, we are able to highlight several points that might
425 assist in the design of an experimental campaign to investigate elements that may be affected by the
426 coupled effects of pressure and sulfur distribution. 1) Datasets should contain experiments covering a
427 wide range of pressures. If all experiments are performed at lower pressures than where ΔV_r^o effects
428 become dominant (i.e., below the inflection points of the curves in Fig 1), accurate extrapolation to
429 higher *P* is not possible; 2) care should be taken to choose *P-T* conditions that do not exaggerate the
430 range in values for R_G, as this may hinder the effectiveness of using *d* in place of a more complex set of
431 fitting parameters; 3) any curvilinear pressure dependence of $\ln D_M^{met/sil}$ will be most readily
432 identifiable from experiments containing similar and relatively high metal S contents. In datasets where
433 the S content varies significantly between experiments, the c_1 term found by regression with (18) tends
434 to be lower than the nominal value; 4) metals that form higher valence species in silicate melt and/or
435 have a greater affinity for complexing with sulfur are expected to show the most dramatic curvilinear
436 pressure dependence. Although consideration of these points may help with regard to accurate
437 parameterization of a dataset by multiple linear regression, suites of experiments designed to probe the
438 effect of individual variables (albeit labor intensive) are still likely to yield the most accurate results.
439

440 **3.2 Application to Literature Data: Gold as a Preliminary Case Study**

441 This study was originally motivated by the apparently conflicting pressure dependencies observed for
442 the metal-silicate partitioning of Au. Righter at al. (2015) perform multiple linear regression of a large
443 experimental database, including both sulfur-bearing and sulfur-free samples, and find that $\ln D_{\mathrm{M}}^{met/sil}$
444 increases with *P*. Conversely, the sulfur-free experiments performed by Bennett et al. (2016) display a
445 decrease in $\ln D_{\mathrm{Au}}^{met/sil}$ with *P*. On the basis of the relationship described above however, this result is
446 expected if Au dissolves into silicate melt at least partly as sulfur-bearing species. Previous studies
447 have shown that Au may indeed form sulfur-bearing species in silicate melt (Botcharnikov et al., 2010),
448 and thus fitting the data with a relationship similar to (18) may yield more accurate extrapolation to
449 pressures beyond the studied range.
450
451 **3.2.1 Regression of Experimental Data.** The experiments performed by Righter et al. (2015) are most
452 useful for the current purpose, being both sulfur-bearing and covering a wide range of pressure. Fig 6a
453 shows the data of Righter et al. (2015) after correction to a constant metal composition (X_{S} = 0.20)
454 using the activity-composition relationship for Au in Fe-Ni-S melts from Jones & Malvin (1990). From
455 Fig 6a it is clear that below 11 GPa, $\ln D_{\mathrm{Au}}^{met/sil}$ increases with increasing *P*, then decreases with
456 increasing *P* from 13 to 23 GPa. This picture is complicated by the fact that the data at 21 and 23 GPa
457 are from experiments done at significantly higher *T* than data from lower pressure experiments (~2700
458 vs ~2000 K). However, applying the temperature dependence found for sulfur-free data (Bennett et al.,
459 2016) to recalculate all the data to a common temperature, the same increase, then decrease, in
460 $\ln D_{\mathrm{Au}}^{met/sil}$ with increasing *P* persists (Fig. 6b). Although this is a crude approach, it suffices to
461 demonstrate that the non-linear change in $\ln D_{\mathrm{Au}}^{met/sil}$ is unlikely to simply be the effect of plotting data
462 at different temperatures together. Also plotted in Fig 6b are the 1 atm sulfur-bearing experiments from
463 Bennett et al., (2016), similarly corrected for metal composition and temperature. These data also
464 appear to support the trend in $\ln D_{\mathrm{Au}}^{met/sil}$ with *P* defined by the Righter et al., (2015) data. The solid

black line in Fig 6b is the best fit trend predicted by (18); generated by constraining b_1 and c_1 to the ranges determined by Bennett et al. (2016) for sulfur-free data, then varying values of a_1, d and n to find the lowest chi-squared value. There are several solutions which yield similar chi-squared values and the gray lines in Fig 6b reflect fits that are equally as good as our best fit at the 95% confidence level.

From Fig 6b it is apparent that a moderately good fit to the data is obtained, however, the highest-pressure data are generally lower than predicted and data at 5-12 GPa are generally underpredicted. It is noteworthy that although Au largely displays the behavior expected on the basis of (18), there are several factors which hinder the application of this relationship to Au partitioning data. First, at reducing conditions, Au solubility and partitioning does not display a strong dependence on fO_2 (Brenan & McDonough, 2009; Bennett et al., 2013; Righter et al., 2015). This is not the behavior expected for the solution of Au as an oxide species and suggests $n = 0$ in the sulfur-free system. If gold also forms sulfur-bearing species in the melt, however, $n \neq 0$ and thus (18) would require amending from its current form in order to be properly applied. Second, it has been suggested that $\gamma_{\mathrm{Au}}^{Sil}$ may change significantly with the sulfur content of the silicate melt (e.g., Botcharnikov et al., 2010). The sulfur contents of silicate melt for the experiments of Righter et al. (2015) are not reported, making it difficult to include a silicate melt activity fitting term. These limitations are best reflected in the fact that acceptable fits to the data require higher values for n (~2-4) than is likely for the oxidation state of Au at these conditions. Despite these limitations, the result shown in Fig 6b is encouraging that (18), or a relationship like it, has utility for fitting metal-silicate partitioning data when the element of interest also forms sulfur-bearing species in the silicate melt.

As discussed in §2.3, at high pressure, sulfur concentrations in the silicate melt become low and

489 $\ln D_{\mathrm{Au}}^{met/sil}$ is predicted to change with pressure in the way expected for the sulfur-free system; i.e. vary
490 on the basis of ΔV_r^o. To test this prediction, Fig 6c displays the high P (≥13 GPa) data of Righter et al.
491 (2015) alongside the sulfur-free data from Bennett et al. (2016) used to constrain the P dependence in
492 that study. Also displayed in Fig 6c is a linear fit to these data with the slope constrained by the sulfur-
493 free pressure dependence found by Bennett et al. (2016). Excellent agreement between these datasets
494 and the sulfur-free pressure dependence is found, suggesting that the sulfur-bearing data of Righter et
495 al. (2015) behave as predicted and thus support the functional form of (18).
496
497 **3.2.2 Application to Core Formation Models.** The metal-silicate partitioning of gold has been used in
498 several studies to constrain the conditions of core segregation in planetary bodies and the requirement
499 for late-accreted material to be added to the terrestrial mantle (e.g., Borisov & Palme 1996; Brenan &
500 McDonough 2009; Bennett & Brenan, 2013; Righter et al., 2015; Bennett et al., 2016). The apparently
501 conflicting pressure dependencies for gold partitioning found by Righter et al. (2015) and Bennett et al.
502 (2016) led the latter authors to perform models using parameterizations of $\ln D_{\mathrm{Au}}^{met/sil}$ from both studies.
503 The maximum metal-silicate equilibration temperature inferred when using these alternative
504 parameterizations differs by ~500 K, somewhat restricting the utility of Au as a magma ocean
505 thermometer. To compare the metal-silicate equilibrium temperatures inferred when using the
506 parameterization for Au derived above *versus* those found previously, we have performed a simple core
507 formation model. We parameterized the database of metal-silicate partitioning experiments for Au
508 compiled by Bennett et al. (2016) using a modified version of (18), in which the $\frac{n}{4}\ln f\mathrm{O}_2$ term is set to
509 0, to account for the fact that previous studies have found this parameter to have a negligible effect on
510 Au partitioning and solubility at reducing conditions. Mantle Au contents were calculated as a function
511 of the mass accreted, with temperature fixed to the liquidus curve determined by Andrault et al. (2011).
512 Similar to previous studies (e.g., Wade & Wood, 2005), the mantle FeO content is increased from

513 X_{FeO}^{sil} = 0.01 to 0.06 throughout accretion, corresponding to an evolution from ~IW-4 to -2. The
514 metal/silicate mass ratio is assumed to be 0.48. Oxygen fugacity as a function of pressure, for use in the
515 Righter et al. parameterization was calculated relative to IW using (23) then converted to absolute fO_2
516 using the pressure dependence of the IW buffer determined by Campbell et al. (2009). Figure 7
517 displays the Au contents of terrestrial mantle calculated using both parameterizations, for both S-free
518 accretion and a scenario where $X_{\mathrm{S}}^{met} = 0.03$; corresponding to the core sulfur contents estimated by
519 McDonough (2003). The final pressure and temperature of equilibration in the model shown are ~29
520 GPa and 2750 K. From Fig. 7, it is clear that differences between the two parameterizations is most
521 prominent during the early stages of accretion, i.e., at low pressure and highly reducing conditions.
522 These conditions favor high sulfur contents in the silicate melt and thus formation of metal-sulfur
523 species in the silicate. At higher pressures, the parameterizations display more similar behavior, in
524 which the difference between S-bearing and S-free curves is essentially due only to activity-
525 composition relations in the metal phase. The primitive upper mantle (PUM) estimate for Au is
526 displayed in Fig. 7 as the grey bar, and reveals that our new parameterization yields PUM values for Au
527 at the conditions outlined above. For models with a higher final equilibration pressure and temperature
528 (i.e., a magma ocean depth that is a greater percentage of the core-mantle boundary depth), Au contents
529 become higher than estimates for PUM. This suggests our new parameterization supports the result of
530 Bennett et al., (2016); that core segregation in a deep magma ocean requires sub-liquidus temperatures
531 to avoid a surfeit of Au in the mantle. We note, however, that the limitations discussed in §3.2.1
532 preclude this from being more than a tentative result.
533

534 **4. Implications**

535 The relationships typically used to parameterize experimentally determined metal-silicate partition
536 coefficients are based on the formation of oxide species and suggest a linear dependence of $\ln D_{\mathrm{M}}^{met/sil}$

on pressure. Several elements, however, have been found to dissolve into silicate melts as both oxide and sulfur-bearing species. We have derived an expression suggesting this can give rise to a non-linear change in $\ln D_{\mathrm{M}}^{met/sil}$ with pressure. In the worst cases, fits using the one-species approach can lead to order of magnitude inaccuracies when predicting the partition coefficient at high *P*. This result has important implications when estimating trace element distribution during metal-silicate equilibrium in a deep magma ocean. Several studies have suggested final metal-silicate equilibration at pressures of 60-80 GPa (e.g., Rubie et al., 2011; Siebert et al., 2013). There are relatively few trace-element partitioning experiments, however, that have been performed at >30 GPa and the majority of the database is populated with much lower pressure data (<20 GPa). In many cases, estimates of the partition coefficient at the high pressures of core-formation therefore require significant extrapolation beyond the experimental conditions. If the relationship used to parameterize the low-pressure data does not have the appropriate functional form, inaccuracies arising from extrapolation will be magnified and the conditions proposed for core-formation on the basis of forward models will be incorrect.

It is plausible that the elements most likely to dissolve as sulfur-bearing species in silicate melt are those that display strongly chalcophile behavior. We have considered Au (both highly chalcophile and highly siderophile) and see that high-pressure and sulfur-bearing experiments show the partition coefficient increases, then decreases, with increasing pressure; meeting the qualitative expectations of our theoretical framework. There are several factors, however, which complicate the quantitative fitting of the Au data (see §3.2.1). Looking ahead, it is important to more rigorously test the veracity of the two-species relationship presented here (eq. 18). One possibility would be to investigate the effect of pressure on $\ln D^{met/sil}$ for Ru, in an isothermal series of sulfur-bearing and sulfur-free experiments. Ru is already thought to form sulfur-bearing species in silicate melt (Laurenz et al., 2013), displays both siderophile and chalcophile behavior, and dissolves into silicate melt as either a 2+ (IW -1.5 to +0.5) or

561 4+ (FMQ -1 to +2) cation (Mann et al., 2012; Laurenz et al., 2013). Ruthenium, and other elements
562 sharing similar properties, should be candidates with which to test for the potential importance of non-
563 linear changes in $\ln D_{\mathrm{M}}^{met/sil}$ with pressure.
564
565 **Acknowledgements**
566 Raul Fonseca and Vera Laurenz are thanked for thoughtful and constructive reviews. Raul Fonseca is
567 also thanked for his editorial handling of the manuscript. James Brenan is thanked for his comments
568 during the incipient stages of this project and Corliss Kin I Sio for helping improve the clarity of the
569 manuscript. Asmaa Boujibar graciously provided her compilation of previous sulfur partitioning data,
570 which was used in-part to formulate the parameterization of sulfur partitioning used in the present
571 study. N.R.B. was supported by the Carnegie Institution of Washington Postdoctoral Fellowship
572 Program, and Y.F. acknowledges support from NSF geochemistry grant EAR-1447311.
573
574 **References**
575 Andrault, D., Bolfan-Casanova, N., Lo Nigro, G., Bouhifd, M. A., Garbarino, G., Mezouar, M. (2011)
576 Solidus and liquidus profiles of chondritic mantle: implication for melting of the Earth across its
577 history, Earth and Planetary Science Letters, 304, 251-259.
578
579 Brenan, J. M., McDonough, W. F. (2009) Core formation and metal-silicate fractionation of osmium
580 and iridium from gold, Nature Geoscience, 2, 798-801.
581
582 Bennett, N. R., Brenan, J. M. (2013) Controls on the solubility of rhenium in silicate melt: Implications
583 for the osmium isotopic composition of Earth's mantle, Earth and Planetary Science Letters, 361, 320-
584 332.

585

586 Bennett, N. R., Brenan, J. M., Fei, Y. (2016) Thermometry of the magma ocean: Controls on the metal-
587 silicate partitioning of gold, Geochimica et Cosmochimica Acta, 184, 173-192.

588

589 Botcharnikov, R. E., Linnen, R. L., Wilke, M., Holtz, F., Jugo, P. J., Berndt, J. (2010) High gold
590 concentrations in sulphide-bearing magma under oxidizing conditions, Nature Geoscience, 4, 112-115.

591

592 Campbell, A. J., Danielson, L., Righter, K., Seagle, C. T., Wang, Y., Prakapenka, V. B. (2009) High
593 pressure effects on the iron-iron oxide and nickel-nickel oxide oxygen fugacity buffers, Earth and
594 Planetary Science Letters, 286, 556-564.

595

596 Chabot, N. L., Agee, C. B. (2003) Core Formation in the Earth and Moon: New experimental
597 constraints from V, Cr and Mn, Geochimica et Cosmochimica Acta, 67, 2077-2091.

598

599 Chabot, N. L., Jones, J. H. (2003) The parameterization of solid metal-liquid metal partitioning of
600 siderophile elements, Meteoritics and Planetary Science, 38,1425-1436.

601

602 Chase, M. W., Davies, C. A., Downey, Jr. J. R., Frurip, D. J., McDonald, R. A., Syverud, A. N. (1985)
603 NIST JANAF Thermochemical Tables Version 1.0, U.S. Dept. of Commerce.

604

605 Corgne, A., Siebert, J., Badro, J. (2009) Oxygen as a light element: A solution to single-stage core
606 formation, Earth and Planetary Science Letters, 288, 108-114.

607

608 Evans, K. A., O'Neill, H. St. C., Mavrogenes, J. A., Keller, N. S., Jang, L. -Y., Lee, J. -F. (2009)
609 XANES evidence for Sulphur speciation in Mn-, Ni- and W- bearing silicate melts, Geochimica et

610 Cosmochimica Acta, 73, 6847-6867.

611

612 Jana, D., Walker, D. (1997) The influence of sulfur on partitioning of siderophile elements, Geochimica
613 et Cosmochimica Acta, 61, 5255-5277.

614

615 Jones, J. H., Malvin, D. J. (1990) A non-metal interaction model for the segregation of trace metals
616 during solidification of Fe-Ni-S, Fe-Ni-P and Fe-Ni-S-P alloys, Metallurgical Transactions B, 21B,
617 697-706.

618

619 Laurenz , V., Fonseca, R. O. C., Ballhaus, C., Jochum, K. P., Heuser, A., Sylvester, P. J. (2013) The
620 solubility of palladium and ruthenium in picritic melts: 2. The effect of sulfur, Geochimica et
621 Cosmochimica Acta, 108, 172-183.

622

623 Laurenz, V., Rubie, D. C., Frost, D. J., Vogel, A. K. (2016) The important of sulfur for the behavior of
624 highly-siderophile elements during Earth's differentiation, Geochimica et Cosmochimica Acta, 194,
625 123-138.

626

627 Li, J., Agee, C. B. (2001) The effect of pressure, temperature, oxygen fugacity and composition on
628 partitioning of nickel and cobalt between liquid Fe-Ni-S alloy and liquid silicate: implications for
629 Earth's core formation, Geochimica et Cosmochimica Acta, 11, 1821-1832.

630

631 Mann, U., Frost, D. J., Rubie, D. C. (2009) Evidence for high pressure core-mantle differentiation from
632 the metal-silicate partitioning of lithophile and weakly-siderophile elements, Geochimica et
633 Cosmochimica Acta, 73, 7360-7386.

634

635 Mavrogenes, J. A., O'Neill, H. St. C. (1999) The relative effects of pressure, temperature and oxygen
636 fugacity on the solubility of sulfide in mafic magmas, Geochimica et Cosmochimica Acta, 63, 1173-
637 1180.
638
639 Métrich, N., Berry, A. J., O'Neill, H, St. C., Susini, J. (2009) The oxidation state of sulfur in synthetic
640 and natural glasses determined by X-ray absorption spectroscopy, Geochimica et Cosmochimica Acta,
641 73, 2382-2399.
642
643 Mungall, J. E., Brenan, J. M. (2014) Partitioning of platinum-group elements and Au between sulfide
644 liquid and basalt and the origins of mantle-crust fractionation of chalcophile elements, Geochimica et
645 Cosmochimica Acta, 125, 265-289.
646
647 Namur, O., Charlier, B., Holtz, F., Cartier, C., McCammon, C. (2016) Sulfur solubility in reduced mafic
648 silicate melts: Implications for the speciation and distribution of sulfur on Mercury, Earth and Planetary
649 Science Letters, 448, 102-114.
650
651 Righter, K., Drake, M. J. (1997) Metal-silicate equilibrium in a homogenously accreting Earth: new
652 results for Re, Earth and Planetary Science Letters, 146, 541-553.
653
654 Righter, K., Drake, M. J., Yaxley, G. (1997) Prediction of siderophile metal-silicate partition
655 coefficients to 20 GPa and 2800 ^{o}C: the effects of pressure, temperature, oxygen fugacity and silicate
656 and metallic melt compositions, Physics of the Earth and Planetary Interiors, 100, 115-134.
657
658 Righter, K. (2011) Prediction of metal-silicate partition coefficients for siderophile elements: An update
659 and assessment of PT conditions for metal-silicate equilibrium during accretion of the Earth, Earth and

660 Planetary Science Letters, 304, 158-167.

661

662 Righter, K., Danielson, L. R., Pando, K. M., Williams, J., Humayun, M., Hervig, R. L., Sharp, T. G.
663 (2015) Highly siderophile element (HSE) abundances in the mantle or Mars are due to core formation
664 at high pressure and temperature, Meteoritics and Planetary Science, 50, 604-631.

665

666 Rose-Weston, L., Brenan, J. M., Fei, Y., Secco, R. A., Frost, D. J. (2009) Effect of pressure temperature
667 and oxygen fugacity on the metal-silicate partitioning of Te, Se, and S: Implications for earth
668 differentiation, Geochimica et Cosmochimica Acta, 73, 4598-4615.

669

670 Rubie, D. C., Frost, D. J., Mann, U., Asahara, Y., Nimmo, F., Tsuno, K., Kegler, P., Holzheid, A.,
671 Palme, H. (2011) Heterogeneous accretion, composition and core-mantle differentiation of the Earth,
672 Earth and Planetary Science Letters, 301, 31-42.

673

674 Sharma, R. C., Chang, Y. A. (1979) Thermodynamics and phase relationships of transition metal-sulfur
675 systems: Part III. Thermodynamic properties of the Fe-S phase diagram. Metallurgical Transactions B,
676 10, 103-108.

677

678 Siebert, J., Corgne, A., Ryerson, F. J. (2011) Systematics of metal-silicate partitioning for many
679 siderophile elements applied to Earth's core formation, Geochimica et Cosmochimica Acta, 75, 1451-
680 1489.

681

682 Siebert, J., Badro, J., Antonangeli, D., Ryerson, F. J. (2013) Terrestrial accretion under oxidizing
683 conditions, Science, 339, 1194-1197.

684

Wade, J., Wood, B. J. (2005) Core formation and the oxidation state of the Earth, Earth and Planetary Science Letters, 236, 78-95.

Wood, B. J., Kiseeva, E. S. (2015) Trace element partitioning into sulfide: How lithophile elements become chalcophile and vice versa, American Mineralogist, 100, 2371-2379.

Figure Captions

Figure 1: The metal-silicate partition coefficient predicted by (18) for a hypothetical 2+ cation at 2500 K and with 20 mol% S in the metal, shown as a function of pressure. Values of a_1, b_1 and c_1 are 1, 10,000 and -50 respectively. The effect of different values for the d parameter are shown by the different curves, as indicated. Note that a value of $d = 0$ suggests that M does not form sulfur-bearing species in the silicate melt and (18) simplifies to (8).

Figure 2: (a, b) The distribution of model data points with respect to T and X_S^{met} as a function of P respectively. Colors correspond to datapoints from the same dataset. **(c)** Values of the coefficients a_1-c_1 relative to their nominal values found by regression of the model data using (8) (blue points) and (18) (red points). **(d)** Model values of $\ln D^{met/sil}$, representative of the measured values in experimental studies, versus the values predicted by (8) and (18). Points are color-coded as for Fig 2c. For references to color, please see the online version of this manuscript.

Figure 3: The nominal pressure dependence of $\ln D_{Bulk}^{met/sil}$ (black curve, calculated using eqs. 8, 10 and 11), alongside that predicted by fits to the model data using (8) (blue curves) and (18) (red curves). It is clear from this figure that fits made using (18) yield a better representation of the nominal pressure dependence.

Figure 4: $\ln D^{met/sil}$ versus P generated using (11) with values for a_9 varied from -4 to +4 as indicated. This represents changing the relative proportions of sulfide versus oxide species in the melt, where decreasing the value of a_9 increases the proportion of sulfide species. As the contribution from sulfide species increases, the degree of curvature also increases.

Figure 5: Values of the parameters a_1-c_1 relative to their nominal values, found by regression of a large number of model datasets. Values are shown versus **(a)** the number of datapoints in each dataset; **(b)** the nominal value of each parameter; **(c)** variation in the range of R_G within a dataset (see main text for details); and **(d)** the range of metal sulfur contents within each dataset. Model data were generated using randomly selected values for the parameters a-c from the ranges stated in Table 1. Blue and red points denote values found using (8) and (18) for the regression respectively.

Figure 6: (a) Values of the metal-silicate partition coefficient for Au found by Righter et al. (2015) as a function of pressure. These values have been recalculated to account for differences in metal composition between runs using the activity-composition relations of Jones & Malvin (1990). With increasing P a slight increase, then large decrease in $\ln D^{met/sil}$ is observed. However, experiments at 21 and 18 GPa were performed at ~600 K higher T than the remainder of the data shown. **(b)** High pressure data from Righter et al. (2015) alongside the 1 atm S-bearing experiments from Bennett et al. (2016). These data have been recalculated to account for differences in metal composition and T, using the T dependence found in the sulfur-free system (see main text for details). Also shown are fits to the data using (18), with the b_1 and c_1 terms constrained by the results of Bennett et al. (2016). The black curve is the best fit (n = 3.55; d = 36.6) and gray curves are those which are similarly good at the 95% confidence level (n_{mean} = 2.95 ±0.58; d_{mean} =53.4 ±20.6). Surprisingly, the single datapoint containing alloy more sulfur-rich than the Fe-FeS eutectic (denoted by the white cross) shows good agreement

734 with more Fe-rich data, which may not be expected based on the behavior of some other HSEs (cf.
735 Laurenz et al., 2016) **(c)** High *P* data from Bennett et al. (2016) alongside data at ≥13 GPa from Righter
736 et al. (2015). Also shown is the sulfur-free pressure dependence from Bennett et al. (2016). Excellent
737 agreement between these data is observed, as expected on the basis of (18), which predicts low S
738 concentrations in the silicate melt at high *P* and thus agreement between the sulfur-bearing and sulfur-
739 free data.
740
741 **Fig 7**: Comparison of mantle Au contents following metal-silicate equilibrium and core-segregation
742 from the base of a magma ocean. Solid lines are results using a parameterization for Au based on
743 equation 18, dashed lines employ the relationship reported by Righter et al., (2015). At low pressures,
744 there are significant differences in the S-bearing models ($X_S^{met} = 0.03$), due to the accounting for
745 sulfur-bearing Au species in the present study. At higher pressures (higher percentage accreted),
746 however, behavior between the different approaches is similar. The grey band shows the range of Au
747 contents estimated for primitive upper mantle.

This is a preprint, the final version is subject to change, of the American Mineralogist (MSA)
Cite as Authors (Year) Title. American Mineralogist, in press.
DOI: https://doi.org/10.2138/am-2018-6282

Figure 1

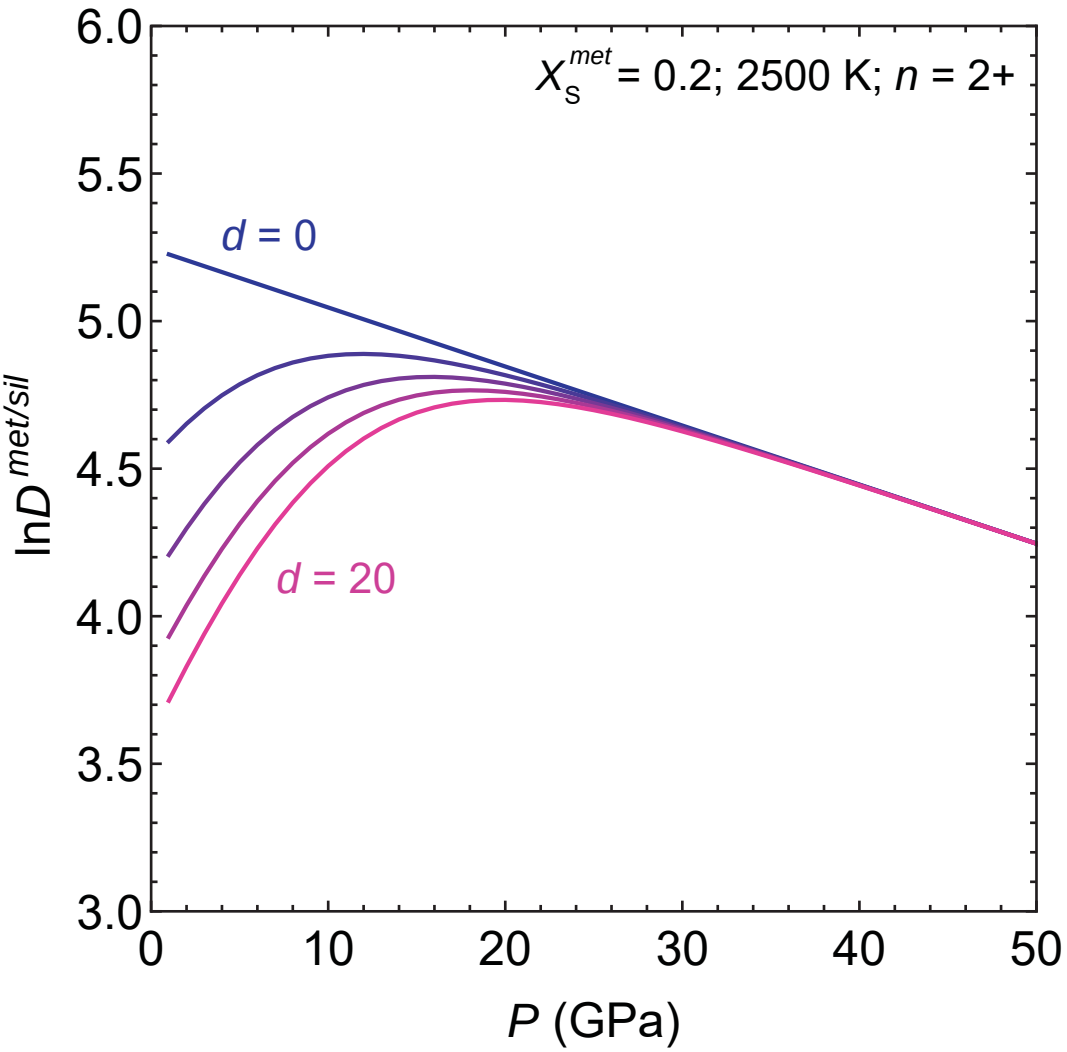

This is a preprint, the final version is subject to change, of the American Mineralogist (MSA)
Cite as Authors (Year) Title. American Mineralogist, in press.
DOI: https://doi.org/10.2138/am-2018-6282

Figure 2

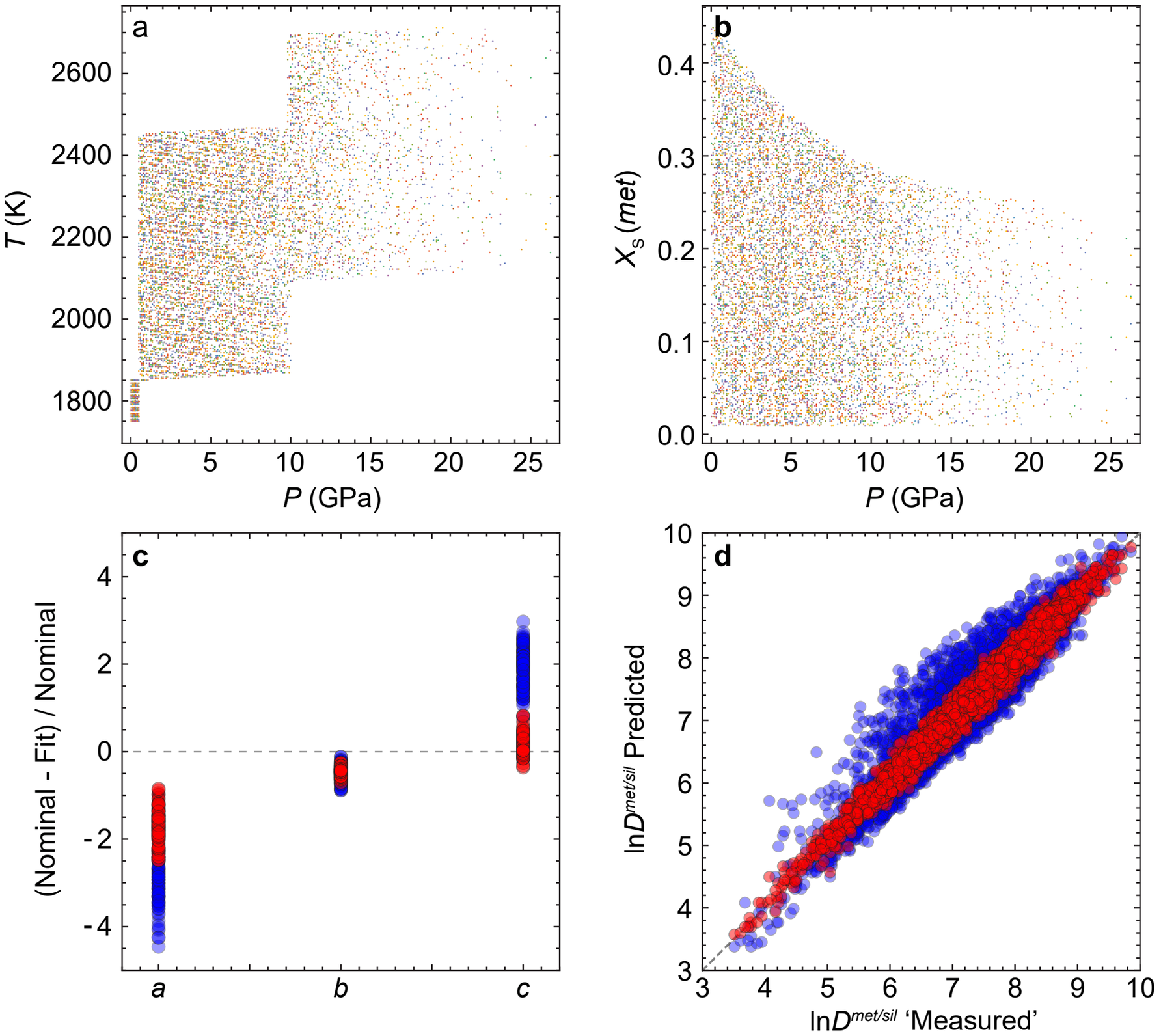

This is a preprint, the final version is subject to change, of the American Mineralogist (MSA)
Cite as Authors (Year) Title. American Mineralogist, in press.
DOI: https://doi.org/10.2138/am-2018-6282

Figure 3

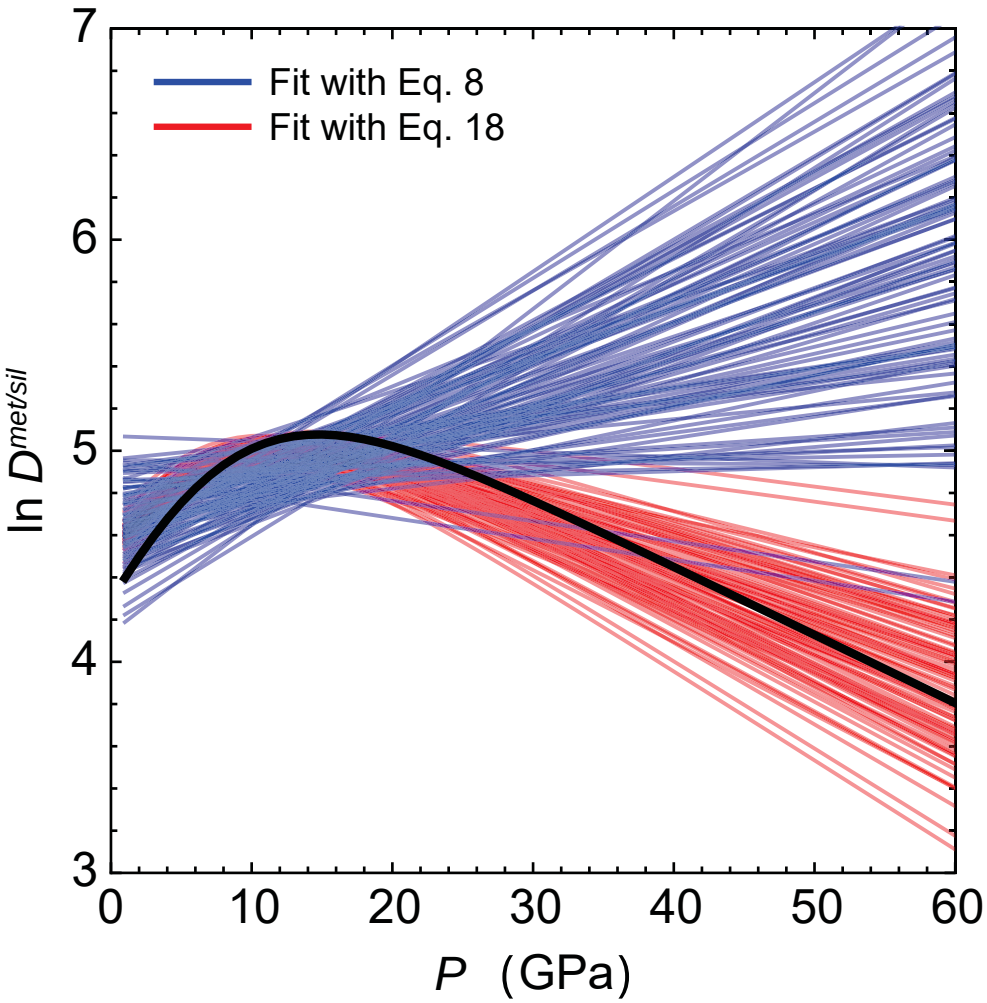

This is a preprint, the final version is subject to change, of the American Mineralogist (MSA)
Cite as Authors (Year) Title. American Mineralogist, in press.
DOI: https://doi.org/10.2138/am-2018-6282

Figure 4

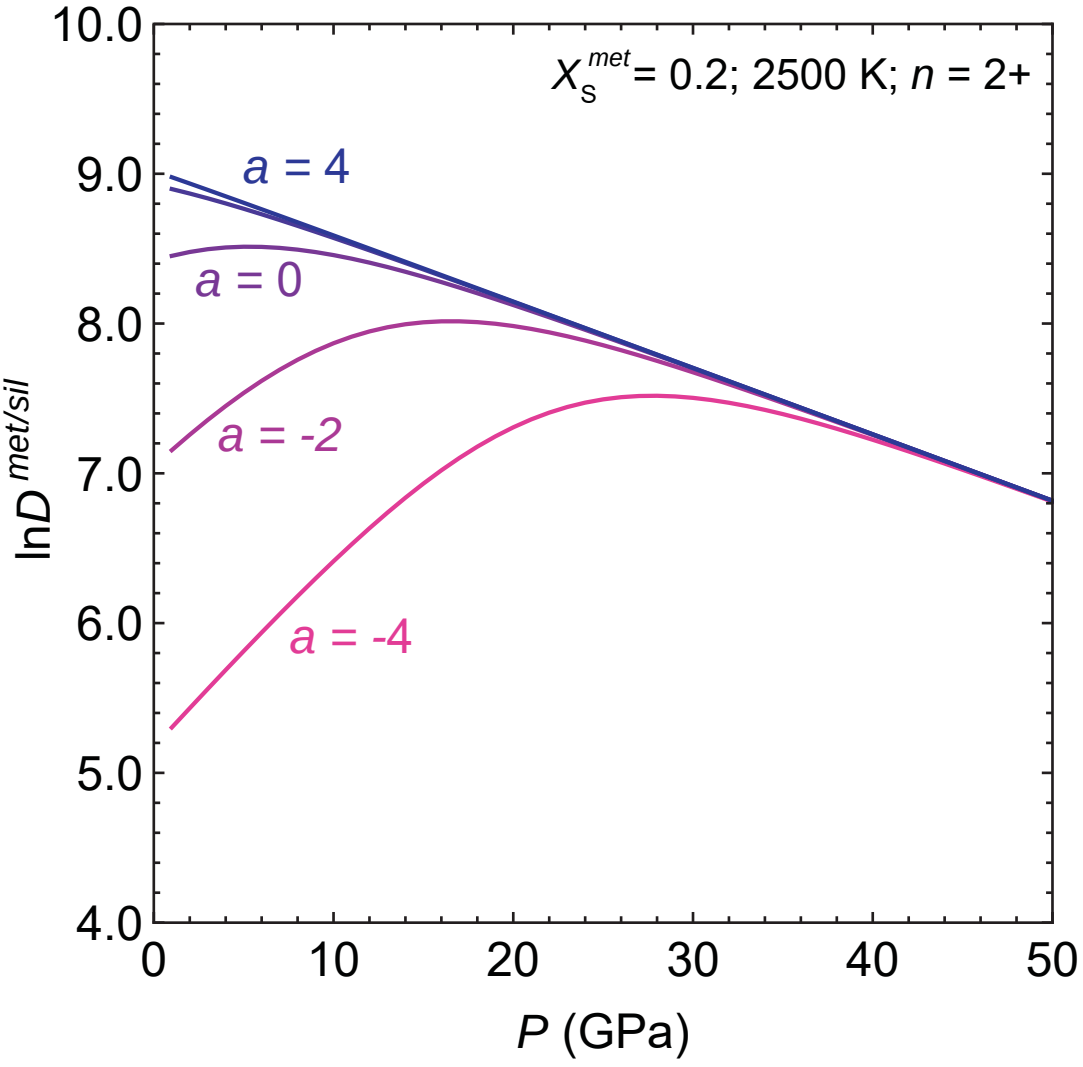

This is a preprint, the final version is subject to change, of the American Mineralogist (MSA)
Cite as Authors (Year) Title. American Mineralogist, in press.
DOI: https://doi.org/10.2138/am-2018-6282

Figure 5

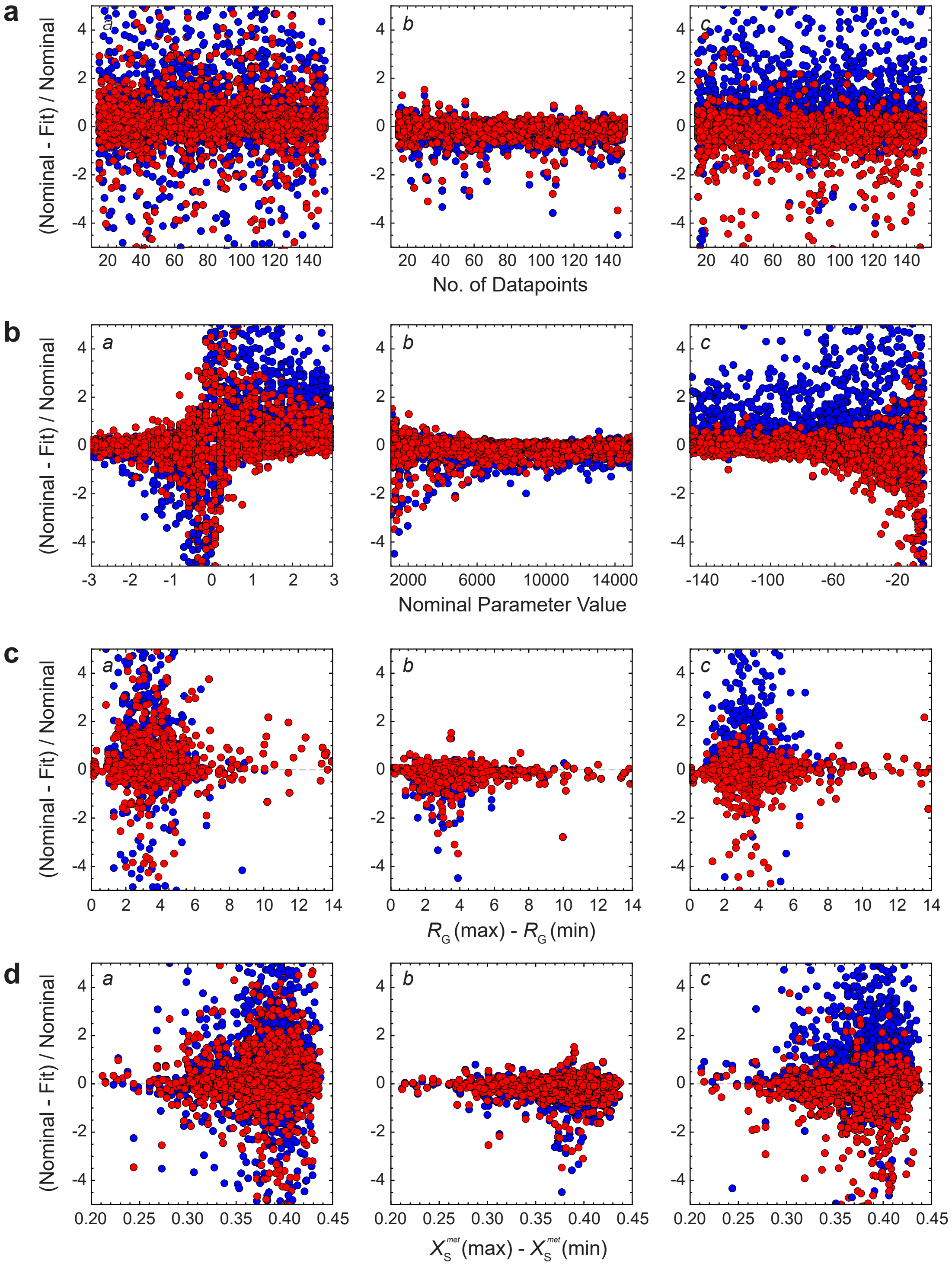

This is a preprint, the final version is subject to change, of the American Mineralogist (MSA)
Cite as Authors (Year) Title. American Mineralogist, in press.
DOI: https://doi.org/10.2138/am-2018-6282

Figure 6

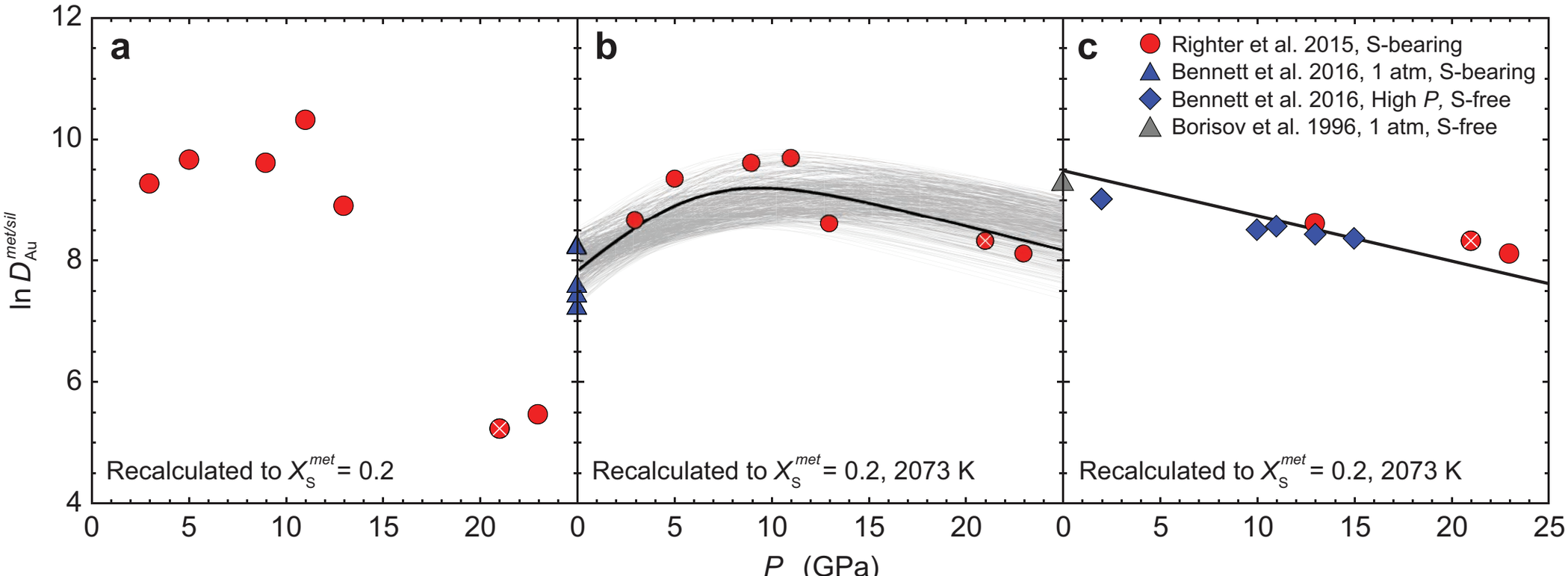

This is a preprint, the final version is subject to change, of the American Mineralogist (MSA)
Cite as Authors (Year) Title. American Mineralogist, in press.
DOI: https://doi.org/10.2138/am-2018-6282

Figure 7

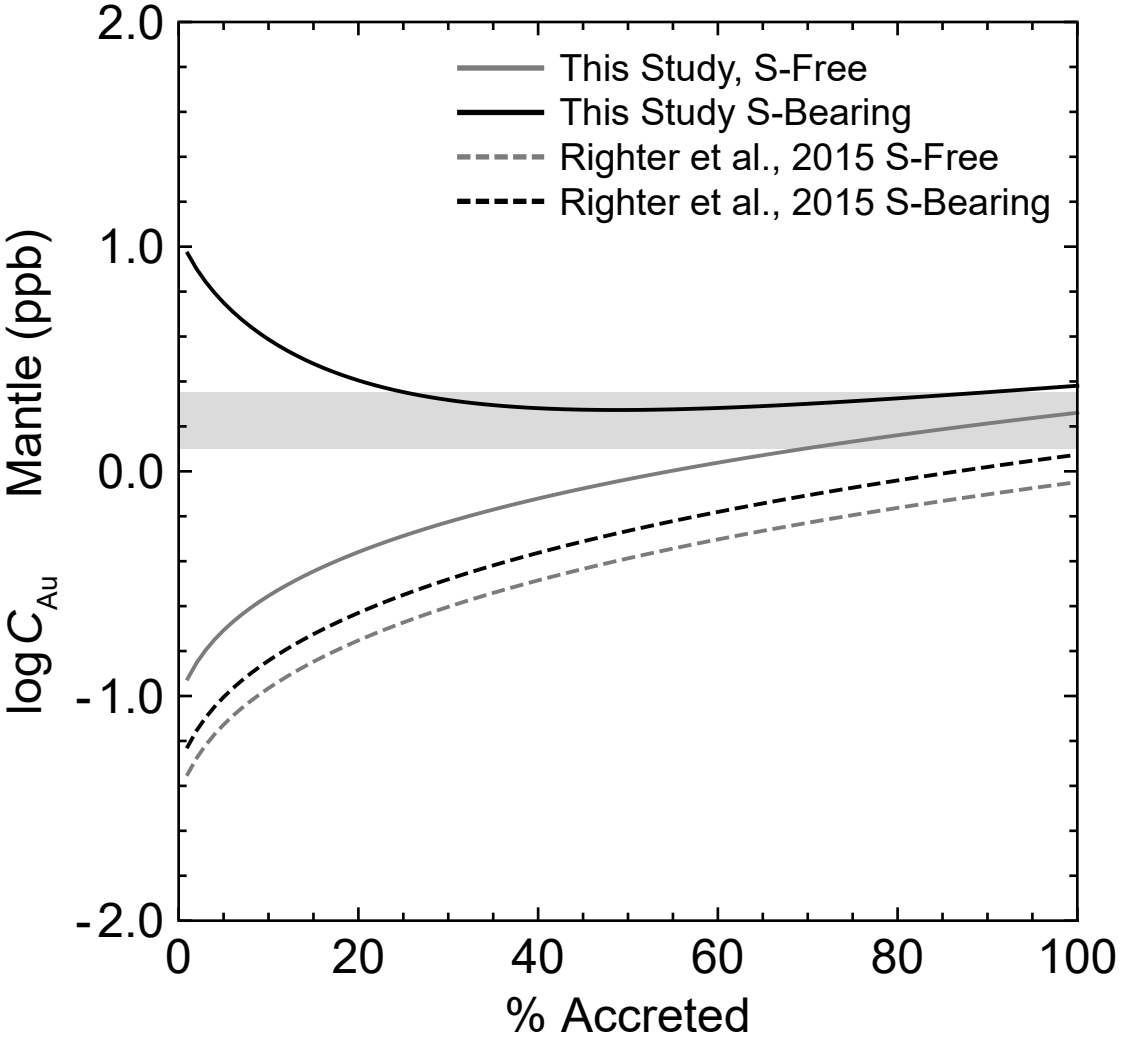

This is a preprint, the final version is subject to change, of the American Mineralogist (MSA)
Cite as Authors (Year) Title. American Mineralogist, in press.
DOI: https://doi.org/10.2138/am-2018-6282

Table 1.

Parameter	Value
a_1	-3 — 3
b_1	1000 — 15000
c_1	-150 — -5
a_9	-3 — 3
b_9	1000 — 15000
c_9	-150 — -5
n (model 1)	2
n (model 2)	1 — 4
β (model 1)	1.5
β (model 2)	0.1 — -1.5
β (Au)	1.082
α	1.09
ω	2
wt to mole conversion factor (FeS)	2.469